

ORIGIN OF TRANSIENT TURBULENT SPOTS IN HYPERSONIC SWEPT BOUNDARY LAYERS WITH MORPHING SWEEP ANGLES

Genrui Jiang[1] & Ming Dong[1]

[1]State Key Laboratory of Nonlinear Mechanics, Institute of Mechanics, Chinese Academy of Sciences, Beijing, China

Abstract

This study investigates the instability and laminar-turbulent transition of a hypersonic swept boundary layer over a plate undergoing dynamic sweep-angle morphing. The morphing motion generates a persistent unsteady base flow that is not captured by steady or quasi-steady interpretations alone. Direct numerical simulations, linear stability theory and secondary instability analysis are combined to identify the origin of transient turbulent spots observed during morphing. The results show that the sweep angle variation produces a slow base-flow wave packet that convects downstream at approximately 0.3 times the freestream velocity and remains active after the structural motion has ceased. A faster crossflow wave packet subsequently overtakes this base-flow perturbation, producing a wave-packet collision that causes strong localised amplification of disturbance energy. In the nonlinear regime, the amplified crossflow vortices saturate earlier and promote high-frequency secondary instability modes, which trigger abrupt laminar breakdown and localised turbulent spots. These spots are accompanied by sharp increases in skin friction and wall temperature, indicating potential thermal protection risks for future hypersonic morphing vehicles.

Keywords: boundary-layer transition, hypersonic flow, crossflow instability, morphing sweep angle, secondary instability

1. Introduction

The development of morphing aircraft operating across multiple flight regimes is driven by the need to maintain aerodynamic efficiency and control authority from the dense atmosphere to near space. Unlike vehicles with fixed geometry, a morphing configuration can actively adjust its planform, sweep angle, wing shape or body contour in response to changing flight conditions [1]. This capability is attractive for future hypersonic systems, yet it also introduces a difficult transition prediction problem. In hypersonic flight, the onset of transition is closely associated with rapid increases in skin friction, wall heat transfer and local thermal loading. Transition prediction is therefore not only a question of aerodynamic drag, but also a key requirement for thermal protection design and structural safety assessment.

Most existing knowledge of swept-boundary-layer transition has been developed for fixed geometries. In such flows, crossflow instability is one of the principal routes to laminar breakdown. The instability originates from an inflectional crossflow velocity profile produced by the imbalance between the pressure gradient and the centrifugal response of the boundary layer. Depending on the external disturbance environment, unstable disturbances may appear as stationary vortices or travelling waves [2, 3]. As the crossflow vortices grow to finite amplitude, they distort the mean flow and form streaky structures. These distorted profiles can then support high-frequency secondary instability modes, which generate small-scale vortical motion and lead to turbulent breakdown [4, 5]. In hypersonic flows, experiments and simulations have shown that crossflow modes, their nonlinear saturation and their secondary instabilities are closely coupled to thermal streaks and wall heat flux amplification [6, 7, 8, 9, 10, 11].

https://doi.org/10.71945/icas2026_0094

Morphing configurations differ fundamentally from fixed geometries. During sweep-angle variation, the boundary layer is not only three-dimensional and spatially developing, but also temporally unsteady. The base flow may retain a memory of the preceding motion after the structural morphing has ceased. The transition process is then path-dependent, since two flows with the same final sweep angle may have different disturbance fields, different stability properties and different wall responses. This feature is particularly important for hypersonic configurations, where localised breakdown may produce transient turbulent spots and intense wall heat flux peaks. A transition prediction based only on the final sweep angle may therefore miss the amplification history that leads to local breakdown.
Theoretical and numerical tools for unsteady instability provide useful guidance, but each has intrinsic limitations for the present problem. Floquet theory is well suited to time-periodic base flows, whereas practical sweep morphing is generally non-periodic. A quasi-steady stability analysis based on frozen base profiles can provide useful local information, especially when the base flow evolves slowly [12, 13]. However, when the sweep angle changes rapidly, the disturbance evolution becomes genuinely spatiotemporal. The relevant question is no longer only whether a given instantaneous profile is unstable, but how the disturbance packet interacts with the evolving base flow over a finite time interval. What remains unclear is how the finite-time history of sweep morphing modifies the route from crossflow amplification to localised turbulent breakdown.
In the present study, we investigate the instability and transition of a Mach 6 swept boundary layer over a blunt plate undergoing dynamic sweep-angle variation. Direct numerical simulations are used to compute the unsteady base flow and to follow the linear and nonlinear evolution of travelling crossflow wave packets. Linear stability theory based on frozen instantaneous profiles is used to identify the local crossflow branches and to clarify the influence of morphing on instantaneous growth. Secondary instability analysis is then applied to saturated crossflow vortices to determine the origin of the high-frequency structures observed in nonlinear simulations. The analysis focuses on the mechanism by which morphing-induced base-flow unsteadiness promotes local amplification, accelerates nonlinear saturation and triggers transient turbulent spots.
The paper is organised as follows. Section 2. introduces the physical model and numerical methods. Section 3. discusses the base-flow hysteresis, the wave-packet collision and the nonlinear transition process. Section 4. summarises the main physical conclusions and their implications for transition prediction in hypersonic morphing configurations.

2. Methodology

2.1 Physical Model

The physical model consists of a blunt swept plate with a semicylindrical leading edge of radius r^*, as sketched in Figure 1. The coordinate frame is rigidly attached to the plate and rotates about the y^* axis, which gives a non-inertial reference frame. The initial sweep angle is denoted by Λ_0, and the final sweep angle after morphing is denoted by Λ_1. During morphing, the instantaneous sweep angle is $\Lambda(t^*)$. The dimensional angular velocity is defined as

$$\Omega^*(t^*) = \frac{\mathrm{d}\Lambda_r(t^*)}{\mathrm{d}t^*}, \qquad \Lambda_r = \frac{\pi}{180}\Lambda, \tag{1}$$

where Λ is measured in degrees and Λ_r is the corresponding angle in radians. The computational region is located at a radial distance z_0^* from the rotation axis. The morphing motion therefore combines rotational and translational effects, with their relative importance determined by z_0^*.
The nose radius r^*, freestream velocity Q_∞, freestream density ρ_∞ and freestream temperature T_∞ are used for nondimensionalisation. The governing parameters are

$$R = \frac{\rho_\infty Q_\infty r^*}{\mu_\infty}, \qquad M = \frac{Q_\infty}{a_\infty}, \qquad \Omega_m = \frac{r^*\Omega^*(t_{\max})}{Q_\infty}, \tag{2}$$

where a_∞ is the freestream sound speed and $t_{\max}$ is the time when the morphing angular velocity reaches its peak. The flow parameters used in the simulations are listed in Table 1.
The dimensionless conservative compressible Navier-Stokes equations in the rotating frame are written as

$$\frac{\partial U}{\partial t} + \frac{\partial F_{c,j}}{\partial x_j} = \frac{\partial F_{v,j}}{\partial x_j} + H, \qquad j = 1,2,3, \tag{3}$$

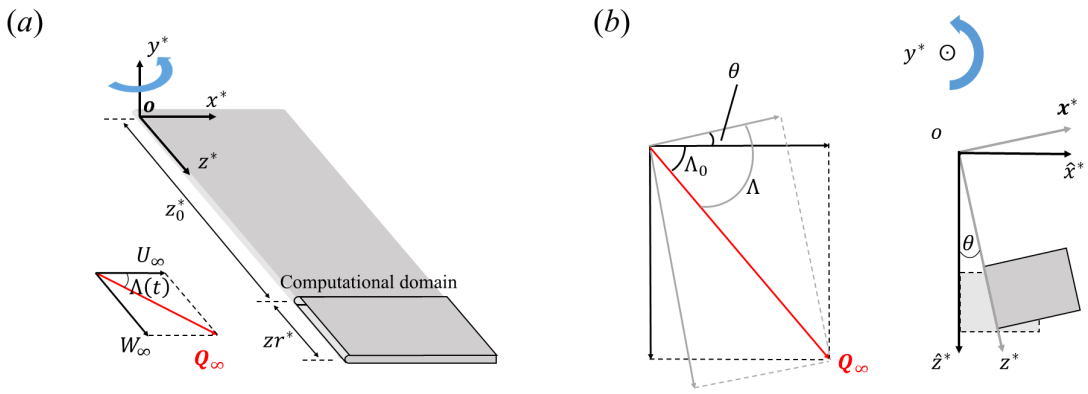


Figure 1 – Schematic of the blunt swept plate and the rotating coordinate frame. (a) 3-D view; (b) Top view.

Mach number	Reynolds number	Freestream temperature	Freestream velocity	Nose radius
M	R	T_∞ (K)	Q_∞ (m/s)	r^* (mm)
6.0	7.91×10^4	226.5	1810	35

Table 1 – Parameters characterising the flow condition.

where repeated indices imply summation. The conservative variable vector is

$$U = [\rho, \rho u_1, \rho u_2, \rho u_3, \rho E]^T, \qquad (u_1, u_2, u_3) = (u, v, w). \tag{4}$$

Here $F_{c,j}$ and $F_{v,j}$ denote the standard inviscid and viscous fluxes of the compressible Navier-Stokes equations. The total energy per unit mass is $E = T/(\gamma(\gamma-1)M^2) + u_i u_i/2$, and the perfect gas equation of state is $p = \rho T/(\gamma M^2)$. The dynamic viscosity follows Sutherland law, $\mu(T) = (1+C)T^{3/2}/(T+C)$, with $C = 110.4\ \mathrm{K}/T_\infty$.
The source term H contains the non-inertial effects induced by sweep angle morphing. In the local spanwise invariant approximation ($z \ll z_0$) used here, the inflow velocity in the rotating frame is

$$u_{in} = (\cos\Lambda - \Omega z_0,\ 0,\ \sin\Lambda + \Omega x)\,. \tag{5}$$

The source term is written as

$$H = H^r + H^a, \tag{6}$$

where

$$H^r = \begin{bmatrix} 0 \\ \rho\Omega^2 x - 2\rho\Omega w - \rho\dot{\Omega} z_0 \\ 0 \\ \rho\Omega^2 z_0 + 2\rho\Omega u + \rho\dot{\Omega} x \\ \rho\Omega^2(xu + z_0 w) + \rho\dot{\Omega}(xw - z_0 u) \end{bmatrix}, \tag{7}$$

and

$$H^a = \begin{bmatrix} 0 \\ \rho\Omega(\sin\Lambda + \Omega x) \\ 0 \\ 0 \\ \rho\Omega(\cos\Lambda - \Omega z_0)(\sin\Lambda + \Omega x) \end{bmatrix}. \tag{8}$$

The first vector contains the centrifugal, Coriolis and Euler acceleration terms, together with their contribution to the total energy equation. The second vector is associated with the local spanwise invariant representation of the morphing flow.

Case	Λ_0 (°)	Λ_1 (°)	Ω_m	z_0	t_3
S1	30	30	0	0	0
S2	60	60	0	0	0
A1	30	60	0.00175	0	310
A2	30	60	0.00523	0	110
A3	30	60	0.01047	0	60
B1	60	30	-0.00523	0	110
C1	30	60	0.00523	30	110

Table 2 – Representative fixed and morphing sweep angle cases.

2.2 Sweep-angle morphing and base-flow computation

The sweep angle evolves from an initial value Λ_0 to a final value Λ_1. The angular velocity is prescribed as a smooth finite time function,

$$\Omega(t) = \begin{cases} 0, & t \le t_0, \\ \dfrac{\Omega_m}{2}\left\{1+\tanh\left[\sigma\left(t-\dfrac{t_1+t_0}{2}\right)\right]\right\}, & t_0 < t \le t_1, \\ \Omega_m, & t_1 < t \le t_2, \\ \dfrac{\Omega_m}{2}\left\{1-\tanh\left[\sigma\left(t-\dfrac{t_2+t_3}{2}\right)\right]\right\}, & t_2 < t < t_3, \\ 0, & t \ge t_3, \end{cases} \tag{9}$$

and the instantaneous sweep angle is

$$\Lambda(t) = \Lambda_0 + \frac{180}{\pi}\int_{t_0}^{t} \Omega(s)\, ds. \tag{10}$$

The base flow $\bar{\phi}(x,y,t) = (\bar{\rho},\bar{u},\bar{v},\bar{w},\bar{T})$ is obtained by solving (3) with the prescribed morphing law. The computation starts from a converged steady swept boundary layer at Λ_0. The angular velocity is then imposed through (9), and the temporal evolution of the base flow is followed until after the morphing motion has ended.

A two step numerical procedure is used. First, the leading edge flow and the bow shock are computed on a domain that includes the blunt nose. The resulting solution supplies the inlet and upper boundary data for a refined near wall domain, where the boundary layer and its instability are resolved with higher accuracy. Convective terms are discretised by high order upwind schemes in the refined domain, viscous terms by central differences, and time integration by an explicit Runge-Kutta method. The wall is no-slip and adiabatic, while the upper boundary and outflow boundary are prescribed from the outer solution and extrapolation, respectively. The refined domain uses a fifth-order upwind scheme for convective terms and a sixth-order central scheme for viscous terms.

2.3 Primary disturbance and linear stability theory (LST)

The disturbance field is defined as

$$\phi'(x,y,z,t) = \phi(x,y,z,t) - \bar{\phi}(x,y,t), \qquad \phi = (\rho,u,v,w,T). \tag{11}$$

For small amplitude disturbances, linearisation of (3) about the unsteady base flow gives

$$\begin{aligned} G\frac{\partial\phi'}{\partial t} + A\frac{\partial\phi'}{\partial x} + B\frac{\partial\phi'}{\partial y} + C\frac{\partial\phi'}{\partial z} + D\phi' + V_{xx}\frac{\partial^2\phi'}{\partial x^2} + V_{yy}\frac{\partial^2\phi'}{\partial y^2} + V_{zz}\frac{\partial^2\phi'}{\partial z^2} \\ + V_{xy}\frac{\partial^2\phi'}{\partial x\partial y} + V_{xz}\frac{\partial^2\phi'}{\partial x\partial z} + V_{yz}\frac{\partial^2\phi'}{\partial y\partial z} = 0. \end{aligned} \tag{12}$$

The coefficient matrices are determined by the instantaneous base flow and by the morphing induced source terms. Their explicit forms follow directly from (3) and are not repeated here.
For local stability analysis, the base flow is frozen at a given streamwise station and time instant. The disturbance is written as

$$\phi'(x,y,z,t) = \frac{\varepsilon}{2}\hat{\phi}(y)\exp\left[\mathrm{i}(\alpha x+\beta z-\omega t)\right]+\mathrm{c.c.}, \tag{13}$$

which leads to the compressible Orr–Sommerfeld (O–S) equations

$$\widetilde{B}\frac{d\hat{\phi}}{dy}+V_{yy}\frac{d^2\hat{\phi}}{dy^2}+\widetilde{D}\hat{\phi}=0. \tag{14}$$

No-slip disturbance conditions and an adiabatic thermal disturbance condition are imposed at the wall, while all disturbance quantities decay at the far-field boundary.

2.4 Direct numerical simulation and secondary instability

Direct numerical simulation (DNS) is used to track the spatiotemporal evolution of crossflow (CF) wave packets on the unsteady base flow. The three dimensional domain is formed by extending the refined boundary layer domain in the spanwise direction. Periodic boundary conditions are imposed in z. At the inlet, a travelling crossflow wave packet is introduced as

$$\phi'(x_0,y,z,t) = \frac{\varepsilon}{2}\hat{\phi}(y)\exp(\mathrm{i}\beta z)\exp\left[-\frac{(t-t_c)^2}{d^2}\right]+\mathrm{c.c.}, \tag{15}$$

where $\hat{\phi}(y)$ is obtained from the local crossflow eigenmode, t_c is the centre time of the packet, and d controls its temporal width. Small amplitude forcing is used to examine linear evolution, while finite amplitude forcing is used to follow nonlinear saturation and breakdown.
The spatiotemporal energy of the linear wave packet is measured using energy norm [14],

$$E(x,t) = \int_0^{2\pi/\beta}\int_0^{\infty}(\phi')^H M_E \phi' \,\mathrm{d}y\mathrm{d}z, \tag{16}$$

where

$$M_E = \mathrm{diag}\left[\frac{\bar{T}}{\gamma M^2\bar{\rho}},\bar{\rho},\bar{\rho},\bar{\rho},\frac{\bar{\rho}}{\gamma(\gamma-1)M^2\bar{T}}\right]. \tag{17}$$

The temporal and spatial envelops are defined by

$$E_t(t) = \max_x E(x,t), \qquad E_x(x) = \max_t E(x,t). \tag{18}$$

Secondary instability analysis (SIA) is applied to the saturated crossflow vortices extracted from the nonlinear simulations. At selected streamwise locations and time instants, the distorted flow is frozen and treated as a two-dimensional periodic base state in the plane normal to the vortex axis. The secondary disturbance is written as

$$\phi_S' = \frac{\varepsilon}{2}\breve{\phi}_S(y,z_v)\exp\left[\mathrm{i}(\tilde{\alpha}_v x_v-\tilde{\omega}t)\right]+\mathrm{c.c.}, \tag{19}$$

where x_v is aligned with the primary crossflow vortex and z_v is the transverse periodic direction. Substitution into the linearised equations gives the compact eigenvalue problem

$$\mathscr{A}\breve{\phi}_S = \tilde{\omega}\mathscr{B}\breve{\phi}_S. \tag{20}$$

This analysis is used to identify the unstable high frequency modes responsible for the small-scale structures observed before the formation of transient turbulent spots.

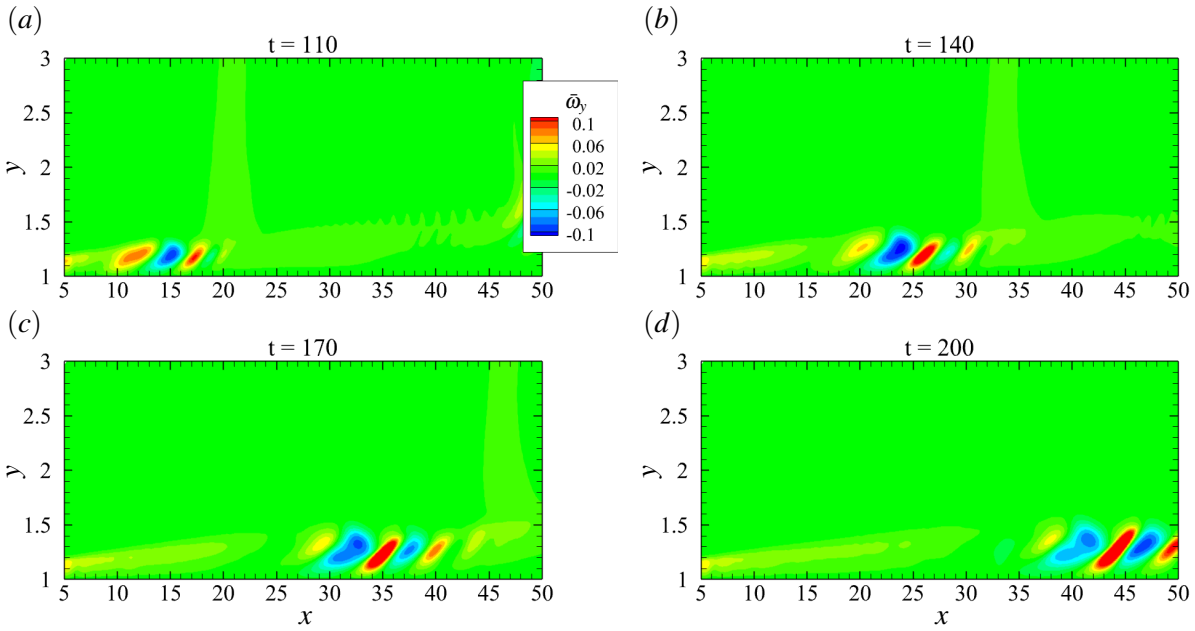


Figure 2 – Contours of the base-flow vertical vorticity $\bar{\omega}_y$ for case A3 at selected time instants. The morphing ceases at $t_3 = 60$.

3. Results and Discussion

3.1 Morphing-induced base-flow unsteadiness

The base flow is first computed without imposed CF disturbances. As the sweep angle increases, the chordwise component of the freestream velocity decreases and the spanwise component increases. For the cases with finite z_0, the translational part of the morphing motion further reduces the effective chordwise velocity through the term $-\Omega z_0$ in equation (5). These changes weaken the bow shock and alter the near-wall velocity profiles.

The most important feature is that morphing generates a base-flow wave packet. Figure 2 shows contours of the base-flow vertical vorticity,

$$\bar{\omega}_y = \frac{\partial \bar{u}}{\partial z} - \frac{\partial \bar{w}}{\partial x}, \tag{21}$$

for the rapid morphing case A3. The wave packet convects downstream at approximately 0.3 times the freestream velocity. Since the morphing motion ends at $t = 60$, while the induced wave packet remains inside the computational domain after this time, the boundary layer exhibits a clear hysteresis effect. The flow therefore continues to evolve after the sweep angle has become fixed at 60°.

Frozen base flow LST clarifies how this hysteresis changes the local instability. Figure 3 shows the spatial growth rate at $x = 20$ during the post-morphing phase of case A3. The corresponding result for case S2 is also included for comparison. When the morphing-induced base-flow packet reaches this location, the growth rate exceeds the steady 60° result. The maximum values are $-\alpha_i = 0.4326$ at $t = 130$ and 0.4166 at $t = 135$, both exceeding the corresponding steady value. By $t = 140$, the instability approaches the fixed-sweep result again. Thus, the local instability is not determined solely by the instantaneous sweep angle, but also by the convective memory of the preceding morphing motion.

3.2 Linear spatiotemporal evolution and wave-packet collision

The frozen profile analysis identifies the local enhancement of CF instability, but the actual disturbance response must be examined through the spatiotemporal evolution of a finite wave packet. DNS is next used to track the evolution of an infinitesimal CF wave packet in the unsteady base flow. The wave packet is introduced during the early morphing phase with $t_c = 5$ and $\beta = 2.0$. As shown in Figure 4, the wave packet energy increases as the sweep angle increases. This trend is consistent with the local stability results, which show that larger sweep angles enhance the instability

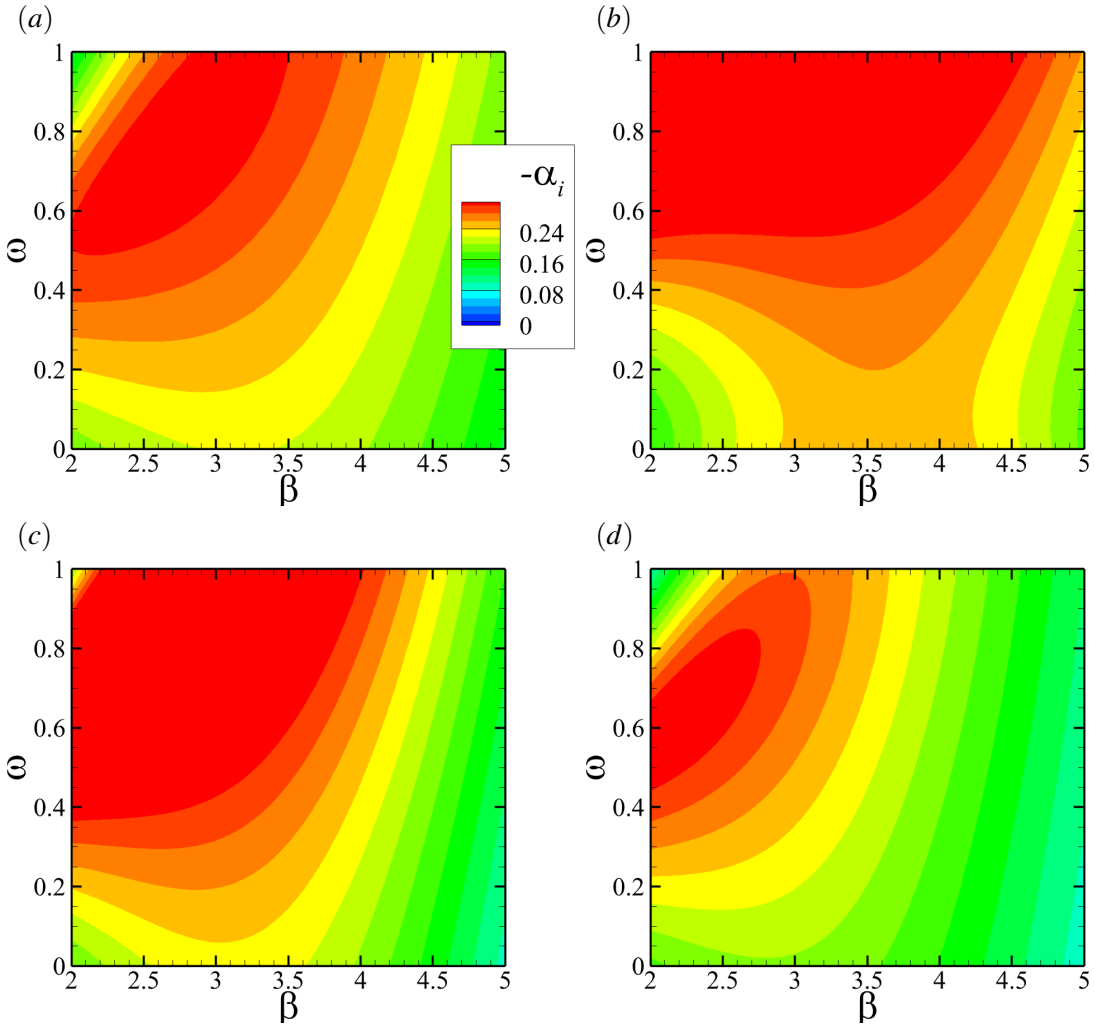


Figure 3 – Contours of spatial growth rate $-\alpha_i$ at $x = 20$ for cases S2 and A3 during the post-morphing phase. (a) Case S2; (b) Case A3 at $t = 130$; (c) Case A3 at $t = 135$; (d) Case A3 at $t = 140$.

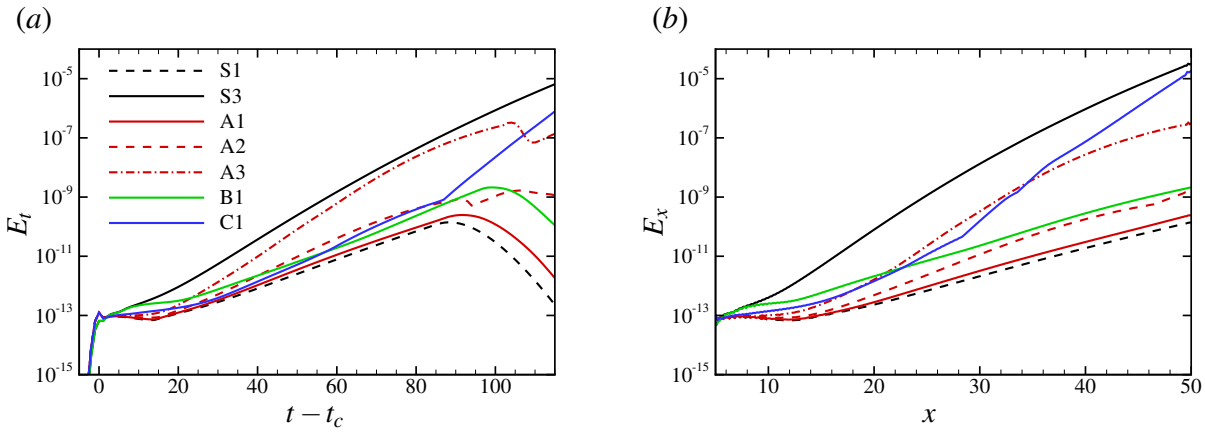


Figure 4 – Temporal (a) and spatial (b) evolution of the wave packet energy for cases S1, S2, A1, A2, A3, B1, and C1, where the parameters for the initial perturbations are $t_c = 5$, $\beta = 2$.

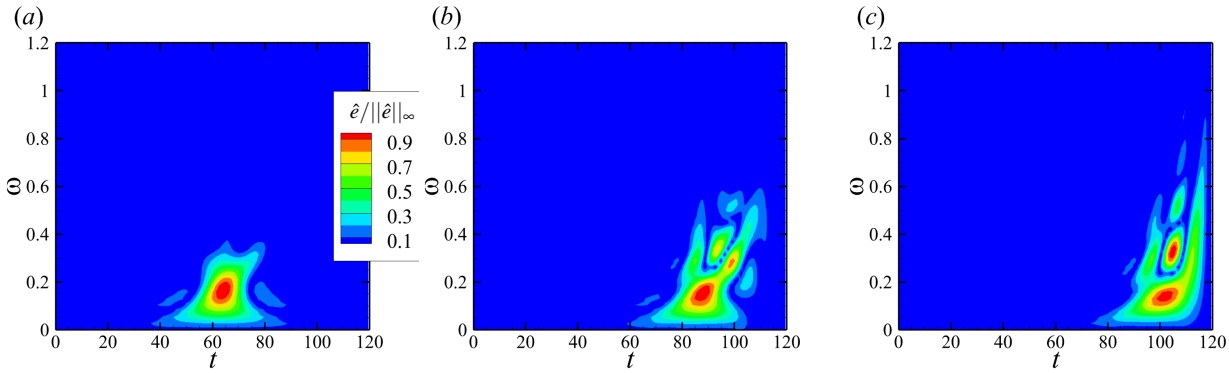


Figure 5 – Normalised WVD spectrum ($\hat{e}/||\hat{e}||_\infty$) in the t-ω domain for case A3 at different chordwise locations. (a) $(x,y,z) = (30, 1.21, 0.314)$; (b) $(x,y,z) = (40, 1.38, 0)$; and (c) $(x,y,z) = (45, 1.39, 0)$. The coordinates y and z at each x are located at the peak of the wave packet.

of CF modes. A faster morphing motion brings the boundary layer to a larger sweep angle within a shorter time, so that the disturbance experiences a more unstable base flow during its downstream propagation. Consequently, the wave packet reaches a higher overall amplitude as the morphing rate increases. In addition to this amplitude enhancement, the packet also undergoes a change in its spectral content and spatial structure. A Wigner-Ville disturbution (WVD) of the velocity signal shows that the dominant frequency increases with morphing strength near $x = 20$, while high frequency components subsequently emerge and grow downstream, as shown in Figure 5.

A more direct view is obtained from the energy contours in the $x-t$ plane (see Figure 6). For fixed sweep conditions, the wave packet spreads while maintaining a coherent convective trajectory. In the morphing cases, the packet trajectory becomes steeper, indicating a reduced group velocity. In case A3, the energy field further develops a two peak structure. This behaviour is consistent with the Wigner-Ville analysis discussed above, where high frequency components emerge during downstream propagation and gradually become energetically significant. The two peaks therefore reflect the coexistence and subsequent separation of different frequency components within the same evolving wave packet.

The key transition-relevant event occurs during the hysteresis phase. Figure 7 compares the temporal and spatial energy envelops for wave packets introduced after morphing has ceased. The CF packet has a group velocity of approximately 0.5 times the freestream velocity, while the base-flow wave packet travels at approximately 0.3. The faster CF packet therefore overtakes the morphing-induced base-flow packet. When this overtaking occurs, the disturbance energy exhibits a distinct kink, followed by a much larger growth rate. This localised interaction is the wave-packet collision mechanism.

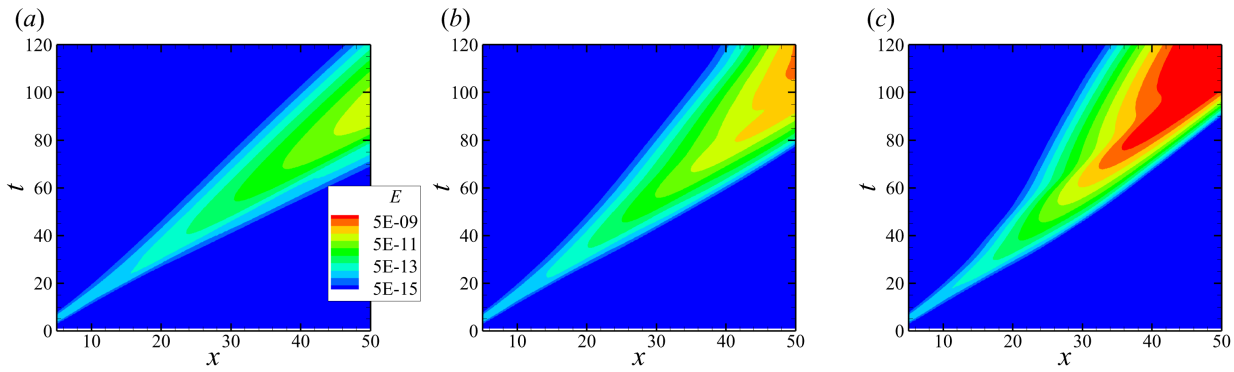


Figure 6 – Contours of the wave packet energy $E(x,t)$ in the x–t plane for cases S1 (a), A2 (b) and A3 (c).

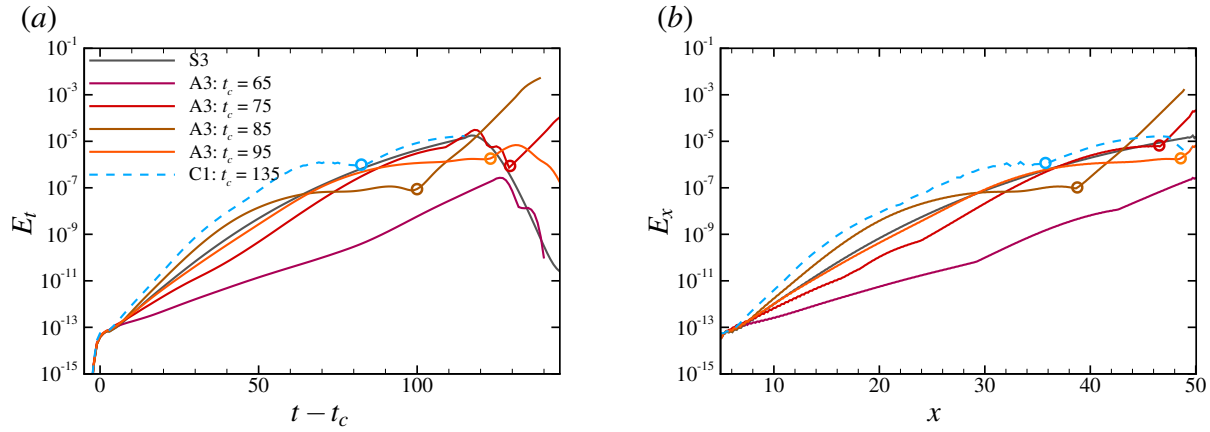


Figure 7 – Temporal and spatial evolution of the linear wave-packet energy for fixed and morphing cases with different introduction times t_c. The kinked points marked by circles indicate wave-packet collision events.

For case A3 with $t_c = 85$, the post-collision energy exceeds the fixed 60° sweep result, even though both flows have the same final sweep angle. The energy increase can reach approximately two orders of magnitude compared with the pre-collision trend. The same mechanism is also observed in case C1, in which translation strengthens the initial morphing-induced wave packet and produces an earlier collision. The collision mechanism is therefore not a numerical artefact of a specific radial position. It reflects a general interaction between the slow base flow unsteadiness and the faster travelling CF disturbance.

3.3 Nonlinear saturation and transient turbulent spots

To determine whether the collision enhanced linear growth can produce transition, finite-amplitude DNS is performed for the representative cases listed in Table 3. The first pair compares early phase forcing for the fixed 30° case S1 and the rapid morphing case A3T1. The second pair compares post-morphing forcing for the fixed 60° case S2 and the rapid morphing case A3T2. The latter pair directly tests the effect of hysteresis and wave-packet collision on nonlinear breakdown.

At early times, the fundamental component follows the linear prediction. When its amplitude reaches $O(0.1)$, nonlinear saturation occurs and the mean-flow distortion and higher harmonics become comparable. In morphing cases, this saturation occurs earlier than in the corresponding fixed-sweep cases, which confirms that morphing-induced amplification shortens the route to the nonlinear regime. Figure 8 compares wall temperature perturbations for S2 and A3T2. Even when the nonlinear amplitude levels are comparable, the morphing case displays more randomised and localised fluctuations, consistent with transient turbulent spots. Because the wall is treated as adiabatic, the temperature perturbation should be interpreted as a thermal response of the boundary layer. For an isothermal wall, the same breakdown process would correspond to localised heat flux amplification.

Case	Sweep angle	Ω_m	ε	t_c	β
S1	30	0	0.02	5	2.0
A3T1	30 to 60	0.01047	0.02	5	2.0
S2	60	0	0.0005	85	3.4
A3T2	30 to 60	0.01047	0.0005	85	3.4

Table 3 – Parameters for nonlinear DNS. The wave packet width is $d = 1.7$ for all cases.

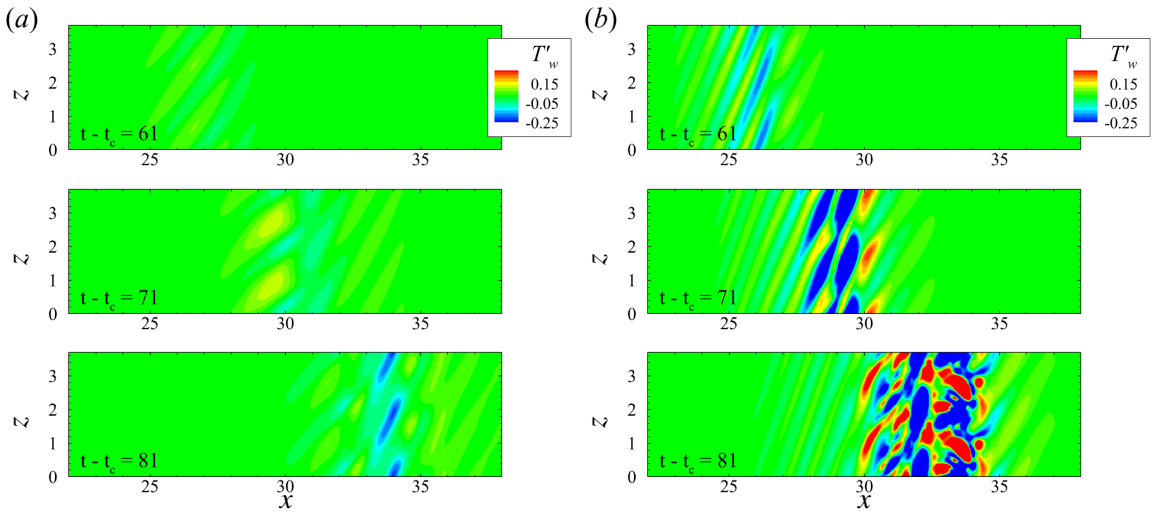


Figure 8 – Contours of wall temperature perturbations T'_w at selected time instants for the fixed 60° case S2 (left column) and the morphing case A3T2 (right column).

The skin friction coefficient provides a second measure of transition impact. It is defined from the spanwise averaged flow as

$$C_f(x,t) = \left(\frac{2\underline{\mu}}{R}\frac{\partial \underline{u}}{\partial y}\right)_{y=0}, \tag{22}$$

with the temporal envelop

$$\|C_f\|_t(x) = \max_t C_f(x,t). \tag{23}$$

As shown in Figure 9, both the mild rise associated with mean-flow distortion and the later sharp rise associated with turbulent spots occur earlier in A3T2 than in S2. The morphing-induced breakdown is therefore not only a disturbance amplitude effect. It also produces a significant advance in the wall loading and thermal response.

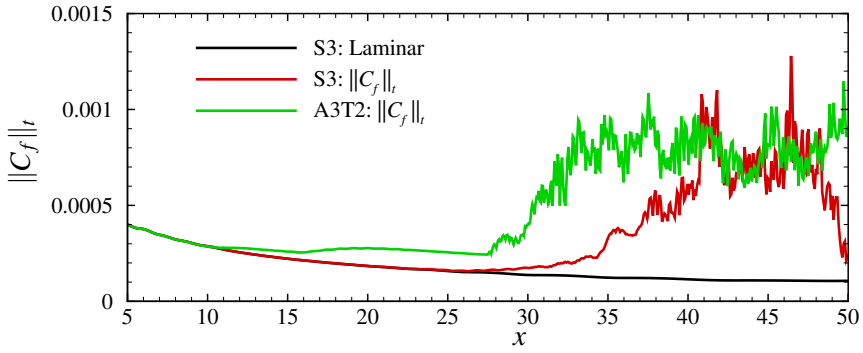


Figure 9 – Chordwise evolution of the skin friction coefficient for cases S2 and A3T2. Solid lines show the temporal envelop, and grey lines show instantaneous distributions.

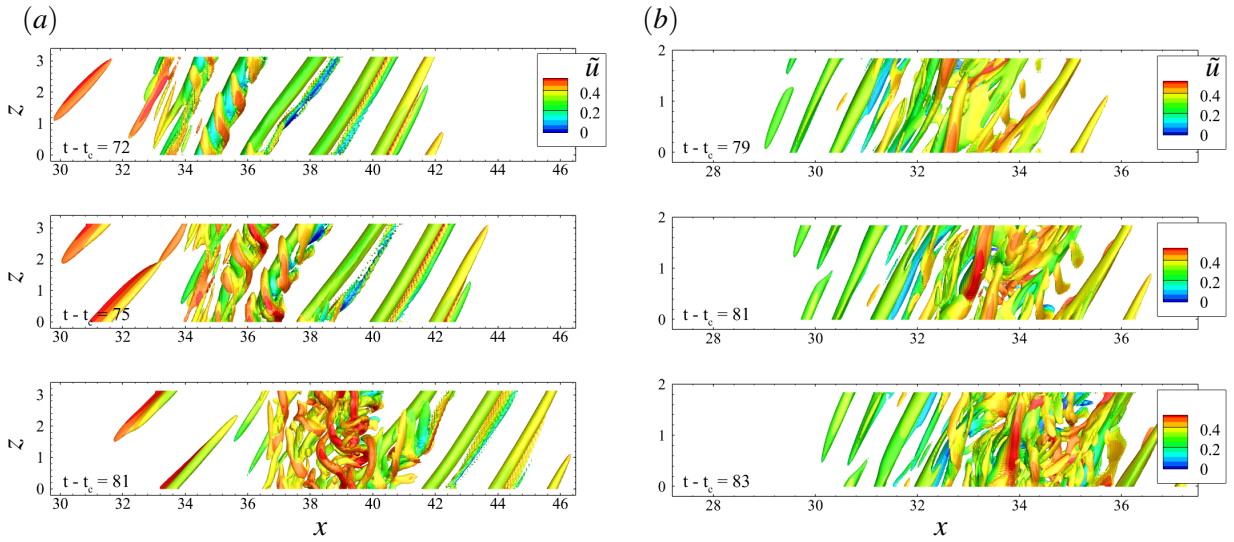


Figure 10 – Visualisation of the instantaneous flow structures of CF vortices during the breakdown phase for cases A3T1 (a) and A3T2 (b) using the Q-criterion with an isosurface level of $Q = 0.08$. The Q-isosurfaces are coloured by the chordwise velocity $\tilde{u}$.

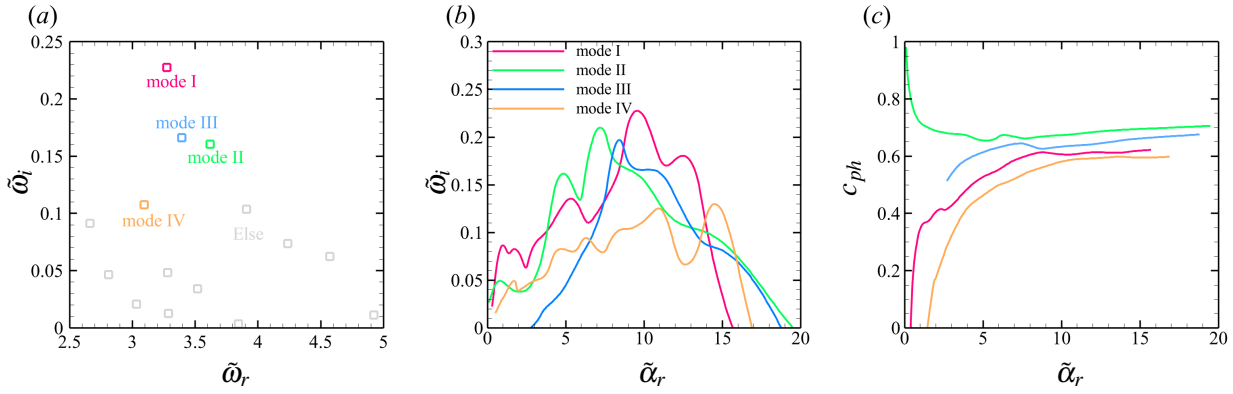


Figure 11 – SI properties for case A3T1 at $x = 35$ and $t = 71$. (a) Eigenvalue spectra for $\tilde{\alpha}_v = 9.6$; (b) growth rate $\tilde{\omega}_i$ vs. wavenumber $\tilde{\alpha}_v$; (c) phase speed c_{ph} vs. wavenumber $\tilde{\alpha}_v$.

3.4 Secondary instability origin of small-scale vortices

The turbulent spots originate from small-scale vortices that appear on the saturated CF structures. DNS visualisations based on the Q-criterion show finger-like vortices wrapped around the primary CF vortex axis (see Figure 10). These vortices intensify rapidly and spread to neighbouring vortex axes, after which the original CF vortices are submerged by chaotic small-scale structures.

SIA explains this rapid growth. The nonlinear CF vortex creates strong wall-normal and lateral shear layers in the vortex-aligned frame. Solving equation (20) for the frozen saturated flow reveals several unstable SI branches with maximum growth rates around 0.23 for representative conditions (see Figure 11). The most amplified SI wavenumber is much larger than the primary CF wavenumber, which justifies the local and quasi-steady treatment used for SIA.

A time-frequency analysis of the DNS signal, shown in Figure 12, separates the low-frequency primary CF contribution from a high-frequency band near $\widetilde{\omega} \approx 4.5$. The latter appears when the small-scale oscillations become visible in the velocity signal. Comparing the extracted high-frequency DNS field with the SIA eigenfunction gives close agreement, as shown in Figure 13. This agreement confirms that the turbulent spots are generated by secondary instability of the saturated CF vortices, rather than by numerical noise or an unrelated high-frequency mode.

The transition route can therefore be summarised as follows. The morphing motion first creates a persistent base-flow wave packet. The CF packet then overtakes this slower base flow disturbance and experiences localised energy amplification. The amplified CF vortices saturate earlier and form

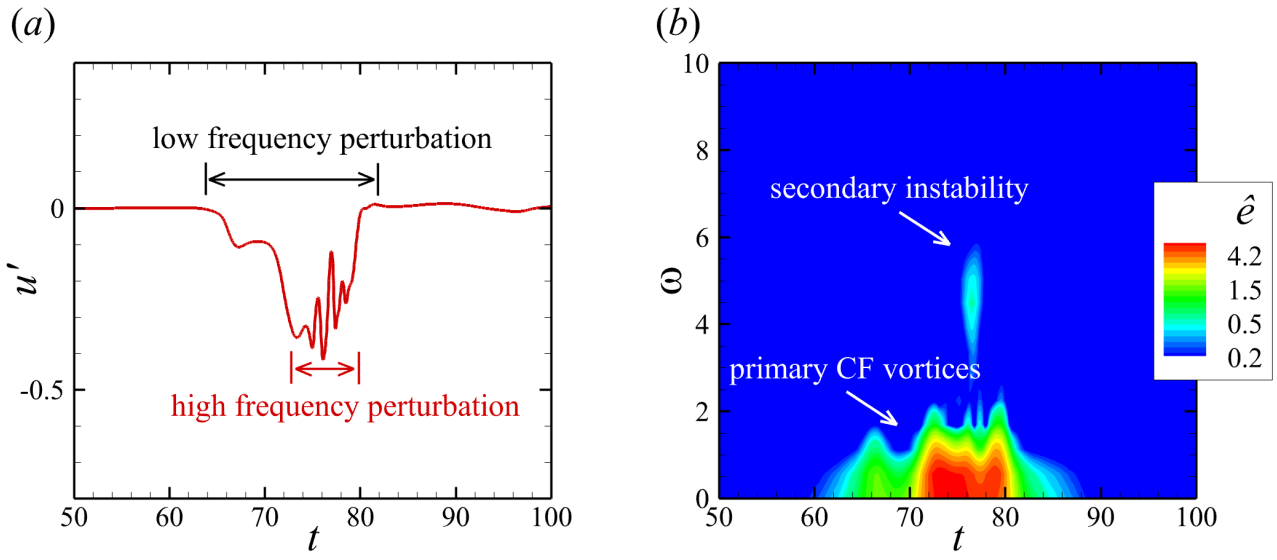


Figure 12 – Identification of high-frequency secondary instability in nonlinear DNS for case A3T1: (a) perturbation velocity signal; (b) smoothed pseudo Wigner-Ville distribution in the time and frequency domain.

stronger streaky distortions. These distorted profiles support rapidly growing SI modes, which generate small-scale vortices and finally transient turbulent spots. This chain connects the macroscopic morphing motion to the localised heating risk observed near the wall.

4. Conclusion

This study investigates the physical origin of transient turbulent spots in a hypersonic swept boundary layer with a morphing sweep angle. DNS, LST and SIA show that dynamic sweep variation produces an intrinsically unsteady transition process that cannot be reduced to a sequence of fixed-sweep states.

The first key result is that morphing generates a slow base-flow wave packet. This packet convects at approximately 0.3 times the freestream speed and persists after the structural motion ends, creating a hysteresis effect in the post-morphing boundary layer. The second key result is that a travelling CF packet moves faster, with a group velocity near 0.5 times the freestream speed. When the CF packet overtakes the base-flow packet, a wave-packet collision occurs. The collision produces a kink in the energy envelop and causes a sharp increase in the CF amplification rate, allowing the disturbance energy to exceed that of the corresponding fixed-sweep case.

The third key result concerns nonlinear breakdown. Collision-enhanced CF vortices reach finite-amplitude earlier, saturate and produce streaky distorted profiles that are highly susceptible to SI modes. The SI modes identified by SIA agree with high-frequency structures extracted from DNS, confirming that the observed turbulent spots originate from secondary instability of saturated CF vortices. These spots produce localised increases in wall temperature and skin friction, and would correspond to heat flux peaks under isothermal wall conditions.

These findings indicate that thermal protection systems for hypersonic morphing vehicles must account for transient overshoot caused by morphing-induced unsteadiness. The final sweep angle alone is insufficient for transition prediction. Instead, the timing, speed and history of the morphing motion must be included, because they determine when the base-flow wave packet interacts with travelling CF disturbances. The present conclusions are based on a prescribed morphing law and an adiabatic wall condition, and future work should examine broader morphing histories and wall thermal models.

5. Contact Author Email Address

Mr. Genrui Jiang: jianggenrui@imech.ac.cn, Prof. Ming Dong: dongming@imech.ac.cn

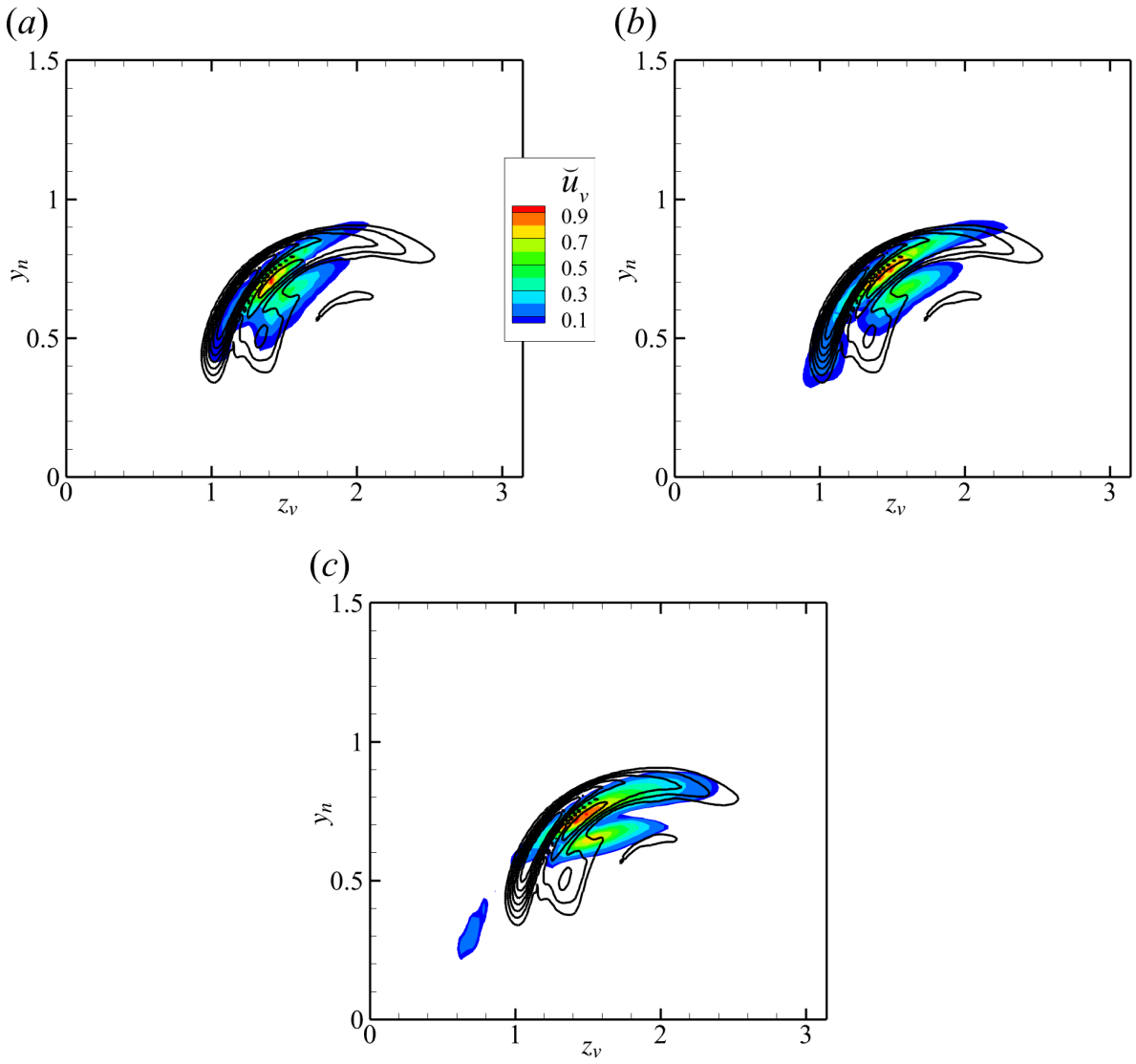


Figure 13 – Comparison of the most unstable SI mode obtained by SIA (solid lines) with the high-frequency component extracted from DNS at $x = 35$ and $\widetilde{\omega} = 4.5$ for case A3T1. (a) $t = 75.5$; (b) $t = 76.5$; (c) $t = 78$.

6. Copyright Statement

The authors confirm that they, and/or their company or organization, hold copyright on all of the original material included in this paper. The authors also confirm that they have obtained permission, from the copyright holder of any third party material included in this paper, to publish it as part of their paper. The authors confirm that they give permission, or have obtained permission from the copyright holder of this paper, for the publication and distribution of this paper as part of the ICAS proceedings or as individual off-prints from the proceedings.

7. Acknowledgements

The work is supported by the National Science Foundation of China (grant nos. 92371104, 12588201, 12372222), the Strategic Priority Research Program, CAS (no. XDB0620102) and the CAS Project for Young Scientists in Basic Research (YSBR-087).

References

[1] S. Barbarino, O. Bilgen, R.M. Ajaj, M.I. Friswell, and D.J. Inman. A review of morphing aircraft. *J. Intell. Mater. Syst. Struct.*, 22(9):823–877, 2011.

[2] H. Bippes. Basic experiments on transition in three-dimensional boundary layers dominated by crossflow instability. *Prog. Aerosp. Sci.*, 35(4):363–412, 1999.

[3] W.S. Saric, H.L. Reed, and E.B. White. Stability and transition of three-dimensional boundary layers. *Annu. Rev. Fluid Mech.*, 35(1):413–440, 2003.

[4] Y. Kohama. Some expectation on the mechanism of cross-flow instability in a swept wing flow. *Acta Mech.*, 66(1):21–38, 1987.

[5] M.R. Malik, F. Li, M.M. Choudhari, and C.L. Chang. Secondary instability of crossflow vortices and swept-wing boundary-layer transition. *J. Fluid Mech.*, 399:85–115, 1999.

[6] T.J. Juliano, M.P. Borg, and S.P. Schneider. Quiet tunnel measurements of HIFiRE-5 boundary-layer transition. *AIAA J.*, 53(4):832–846, 2015.

[7] M.P. Borg, R.L. Kimmel, and S. Stanfield. Traveling crossflow instability for the HIFiRE-5 elliptic cone. *J. Spacecr. Rockets*, 52(3):664–673, 2015.

[8] C. Ward, R. Henderson, and S.P. Schneider. Secondary instability of stationary crossflow vortices on an inclined cone at mach 6. *AIAA Paper*, 2015. 2015–2773.

[9] S.A. Craig and W.S. Saric. Crossflow instability in a hypersonic boundary layer. *J. Fluid Mech.*, 808:224–244, 2016.

[10] F. Li, M. Choudhari, P. Paredes, and L. Duan. High-frequency instabilities of stationary crossflow vortices in a hypersonic boundary layer. *Phys. Rev. Fluids*, 1(5):053603, 2016.

[11] A.J. Moyes, P. Paredes, T.S. Kocian, and H.L. Reed. Secondary instability analysis of crossflow on a hypersonic yawed straight circular cone. *J. Fluid Mech.*, 812:370–397, 2017.

[12] H.J. Obremski and M.V. Morkovin. Application of a quasi-steady stability model to periodic boundary-layer flows. *AIAA J.*, 7(7):1298–1301, 1969.

[13] J. Luo and X. Wu. On the linear instability of a finite stokes layer: instantaneous versus floquet modes. *Phys. Fluids*, 22(5), 2010.

[14] B.T. Chu. On the energy transfer to small disturbances in fluid flow (Part I). *Acta Mech.*, 1(3):215–234, 1965.